Full Length Article

Validation of synergistic effect in N—C@SnO$_2$ hollow nano-microspheres through interfacial chemical bonding for boosting electrochemical sensing

Kungang Chai [a], Shizhao Zhang [a], Hongjie Liu [a], Shaopeng Wang [b,c], Zhenghua Chen [b], Kefu Yu [b,d], Liwei Wang [b,c,d,*]

[a] School of Chemistry and Chemical Engineering, Guangxi University, Nanning 530004, China
[b] School of Marine Sciences, Coral Reef Research Center of China, Guangxi Laboratory on the Study of Coral Reefs in the South China Sea, Guangxi University, Nanning 530004, PR China
[c] School of Resources, Environment and Materials, Guangxi Key Laboratory of Processing for Non-ferrous Metallic and Featured Materials, Guangxi University, Nanning 530004, China
[d] Southern Marine Science and Engineering Guangdong Laboratory (Zhuhai), Zhuhai 519080, China

A B S T R A C T

Higher resistance is exceptionally detrimental to metal oxide-based electrochemical sensors' detection performances that depend on their electrical conductivity. Herein, guided by the synergistic effect of the heterophase boundary, a hollow core–shell combination with a double-layered structure was engineered via hydrolysis strategy, namely nitrogen-doped carbon hollow nano-microspheres (N—C HNMs) coated with SnO$_2$ outer layer (N—C@SnO$_2$ HNMs), then applied for high-performance electrochemical sensing. Advantages including large surface area and strong electronic coupling of Sn-C bond on the boundary facilitated the adsorption of target molecules and electron transferring across the composites, achieving efficient quantitative identification. Density functional theory (DFT) calculation demonstrated the motivation of the charge accumulation at the interface due to the formation of the Sn-C bond, which acted as a bridge for charge transfer. Unsurprisingly, the N—C@SnO$_2$ HNMs-based electrode showed an excellent performance toward dopamine (DA), such as favorable DA selectivity, a lower limit of detection, and a wide linear detection range. Moreover, the electrode material could be applied to the microsensor for *in-situ* DA detection in artificial sweat.

1. Introduction

Dopamine, a significant biomolecule distributed in the human body, plays a potential role in the physiological system. The abnormal DA level is the key to diagnose various diseases, such as Parkinsonism, schizophrenia, and scurvy [1–3]. In conclusion, detecting DA is meaningful and essential in diagnosing, preventing, and treating the above diseases. Unlike the difficult-to-operate, time-consuming, expensive mass spectrometry [4] and liquid chromatography [5], the electrochemical sensor has recently attracted considerable attention owing to its advantages of favorable convenience, reliable selectivity, low limit of detection (LOD), and short-time response compared to other analytical methods. Accordingly, the electrochemical sensor has been extensively explored for many applications such as drug control [6], environmental assessment [7], foodborne pathogens detection [8,9], biological monitoring [10], and health examination [11].

Electrode materials, the clincher to decide the electrochemical property, has various types such as carbon material [12,13], noble metal [14], metal–organic framework [15], polymer [16], metal oxides [17], and so on. For a long time, metal oxide-based catalysts have held great promise as a catalyst for electrochemical sensors due to their abundant active sites, enhanced catalytic properties, and remarkable stability [18,19,20,21,22]. Yet, their intrinsically poor conductivity is one of the major obstacles in electrochemical detection, leading to the relatively lower sensitivity and higher LOD [23]. Therefore, the current electrode materials need to be modified reasonably to improve the performance of electrochemical sensors. Carbon, one of the most abundant elements in nature, can be utilized as conductor material to enhance the electrical conductivity of the compound substrate. To date, an inordinate variety of carbon materials have been advocated for electrochemical detection, such as carbon nanotubes [24], reduced graphene oxide [25], graphene quantum dots [26], and so on. Despite multiple methods that have been

employed to combine the conductive carbonaceous materials and the metal oxides, the weak interface chemical coupling between metal oxides and carbon still causes a sizeable charge-transfer barrier, thus delivering unsatisfactory electrochemical properties [27]. Therefore, an effective method is urgently needed to enhance the interfacial coupling effect to improve redox kinetics and electrochemical sensing performance.

Currently, many methods exist to prepare the composites with the intense interfacial-coupling action between the heterogeneous interface, enabling the electrons to traverse rapidly through the chemical bond. For example, due to the improved charge transfer, the reported SnSe$_2$@C with the Sn-C chemical bond delivered a superior rate capability and good cycling stability of sodium-ion batteries [28]. Following a similar process, the growth of MoSe$_2$ sheets on graphene by Mo-C bond facilitates electrons across the interface, suggesting fast pseudocapacitive Na-ion storage with excellent durability over many cycles [29]. Thus, the strong interfacial electronic coupling could be a key factor for the electron transfer to enhance the redox kinetics, leading to better electrochemical performances [30].

Herein, an interfacial synergistically effect guided scheme was reported to coat SnO$_2$ outer-layer on the nitrogen-doped carbon hollow nano-microspheres via hydrolysis strategy, named N—C@SnO$_2$ HNMs. The introduction of conductive N—C HNMs as inner-supporter could effectively improve the electrical conductivity of the bare SnO$_2$ HNMs and enhance the charge transfer between the hybrid phases of SnO$_2$ and N—C HNMs through the interfacial Sn-C bond. For this reason, the N—C@SnO$_2$ HNMs exhibited enhanced electrochemical properties, such as a lower LOD (41.5 nM) and a wider linear detection range from 0.5 to 90 μM. DFT calculations and XPS results demonstrated the role of charge accumulation at the interface of N—C@SnO$_2$ HNMs. Last but not least, such hybrid electrode material was applied to a microsensor for *in situ* DA detection through assembling with the microchip, thus holding a significant promising practical and rapid clinical diagnosis.

2. Experimental section

2.1. Materials

L-Cysteine (Cys), uric acid (UA), and potassium stannate trihydrate (K$_2$SnO$_3$·3H$_2$O) were purchased from Aladdin Industrial Inc.; Tetraethyl orthosilicate, urea, L-glutathione reduced (GSH), and glucose (Glu) were purchased from Macklin Inc.; L-Ascorbic acid (AA) was purchased from Sinopharm Chemical Reagent Co., Ltd.; Dopamine was purchased from Xiya Regent Science and Technology Co., ltd.; Ethanol and sodium hydroxide (NaOH) were purchased from Chron Chemicals Co., ltd. All chemicals were used as received without any further purification.

All the electrodes were purchased from Tianjin Aida Hengsheng Technology Development Co., ltd. The microsensor was purchased from Guangzhou Mecart Sensor Technology Co., ltd.

The artificial sweat was supplied by Nanning Municipal Center for Disease Control. The entire experimental process will not involve ethical issues.

2.2. Synthesis of the N—C@SnO$_2$ HNMs

In a typical synthesis, SiO$_2$ nano-microspheres were prepared by the Stöber method [31] and used in the following experiments. 0.1 g of SiO$_2$ nano-microspheres were dispersed in 10 mL of deionized water, and then 75.6 mg of DA was added. After gently stirring for 18 h, the obtained brown powder was collected by centrifugation and dried overnight in a vacuum oven at 60 °C. Then, 90 mg of the obtained SiO$_2$@ Polydopamine (PDA) core@shell nano-microspheres, 144 mg of K$_2$SnO$_3$·3H$_2$O and 0.9 g of urea were dispersed in a solution of 18 mL of deionized water and 12 mL of ethanol under ultrasound. The suspension was transferred to 50 mL of Teflon-lined stainless steel autoclaves and heated at 170 °C for 36 h to obtain the SiO$_2$@PDA@SnO$_2$

core@shell@shell nano-microspheres, and then the powder was carbonized at 800 °C for 2 h in the argon atmosphere to obtain the SiO$_2$@N—C@SnO$_2$ core@shell nano-microspheres [32]. Finally, the SiO$_2$ cores were etched off in 2.0 M NaOH aqueous solution to obtain the double-shell N—C@SnO$_2$ HNMs.

2.3. Synthesis of the SnO$_2$ HNMs

For comparison, SnO$_2$ HNMs were synthesized. In a typical synthesis, 0.1 g of SiO$_2$ nano-microspheres, 144 mg of K$_2$SnO$_3$·3H$_2$O and 0.9 g of urea were dispersed in the solution of 18 mL of deionized water and 12 mL ethanol under ultrasound. The suspension was subsequently transferred to 50 mL of Teflon-lined stainless autoclaves and heated at 170 °C for 36 h to obtain the SiO$_2$@SnO$_2$ HNMs. After washing deionized water and ethanol, the SiO$_2$ cores were etched off in 2.0 M NaOH aqueous solution to prepare the SnO$_2$ HNMs.

2.4. Synthesis of the N—C HNMs

In a typical synthesis, 0.1 g of SiO$_2$ nano-microspheres was dispersed in 10 mL deionized water and added 75.6 mg of DA. After slow stirring for 18 h, the obtained brown powder was collected by centrifugation and dried overnight in a vacuum oven at 60 °C. The brown powder was carbonized at 800 °C for 2 h in the argon atmosphere to obtain the SiO$_2$@N—C core@shell nano-microspheres. Then, the SiO$_2$ cores were removed by 2.0 M aqueous NaOH solution to produce final N—C HNMs.

2.5. Characterization and electrochemical measurement

The samples were characterized by employing powder X-ray Diffraction (XRD) analysis (Rigaku Ultima IV, Cu Kα radiation, λ = 1.5418 Å, Japan), Field-emission Scanning Electron Microscope (SEM) (Hitachi SU5000, Japan), Transmission Electron Microscope (TEM) and High-Resolution Transmission Electron Microscope (HRTEM) with Energy dispersive spectrometer (EDS) (FEI TeN-Cai G2 f20 s-twin, 200 kV, USA), X-ray Photoelectron Spectroscopy (XPS) (Thermo SCIENTIFIC ESCALAB 250Xi, Al Kα X-ray monochromator, USA), UV/Vis/NIR spectrophotometer (PerkinElmer, LAMBDA 1050+, USA), BET (Autosorb-IQ, USA), DSC-TG (STA 409 PC, NETZSCH, Germany).

The electrochemical experiments were performed using an electrochemical work-station of VERTEX C (IVIUM, Netherlands). The modified glassy carbon electrode (GCE) was used as working electrode (WE). A Pt foil and Ag/AgCl (3 M KCl) served as the counter (CE) and reference (RE) electrode, respectively. The experiments were conducted in a 0.1 M phosphate buffer solution (PBS, pH = 7.4). The electrochemical measurements were carried out via cyclic voltammetry (CV), square wave voltammetry (SWV), and electrochemical impedance spectroscopy (EIS). The CV measurements were performed over a potential range from 0 to 0.4 V at a scan rate of 50 mV s^{-1}. The SWV conditions used were step height of 2 mV, frequency of 25 Hz, and pulse height of 25 mV. EIS measurements were carried out in a 5 mM [Fe(CN)$_6$]$^{3-/4-}$ solution containing 0.1 M KCl. Its frequency range was set from 0.1 Hz to 100 kHz, using an amplitude of 5 mV. The FR-4 Printed three-electrode using gold as the working electrode, carbon electrode as counter electrode and Ag/AgCl as the reference electrode.

2.6. Preparation of modified GCEs

For the preparation of electrodes, SnO$_2$ and N—C@SnO$_2$ HNMs (5 mg) were ultrasonically dispersed in a mixture solution of ethanol and nafion (1 mL) for 30 min. Before modification, the GCE (5 mm in diameter) was polished sequentially with 5.0, 0.5, and 0.03 μm of Al$_2$O$_3$ powder and then washed ultrasonically in distilled water. Then, a drop of the suspension (5 μL, 5 mg mL^{-1}) was covered on the surface of polished GCE and dried at room temperature. The loading catalyst on the GCEs is about 0.25 mg cm^{-2}.

2.7. DFT calculations

In this work, the DFT calculations were performed by using the Vienna ab initio simulation package [33,34] (VASP) with the projector augmented wave (PAW) potentials. The Perdew-Burke-Ernzerhof (PBE) level of the generalized gradient approximation (GGA) was adopted to optimize the structures (i.e., SnO_2, $SnO_2(1\,1\,0)$, N—C, $SnO_2(110/N$—C)). The Brillouin zones were sampled by a Monkhorst-Pack k-point mesh with a $2 \times 4 \times 1$ grid for $SnO_2(1\,1\,0)/N$—C. The plane wave cutoff was set to 450 eV. The electron convergence energy was set to 10^{-5} eV and the proposed atomic positions were allowed to relax until the forces were less than 0.02 eV/Å. A vacuum layer of 15 Å along the z-axis was used to avoid periodic image interactions.

3. Results and discussion

3.1. Characterization

The synthesis process of N—C@SnO_2 hollow nano-microspheres (HNs) was schematically illustrated in Fig. 1. According to the SEM images, the as-prepared SiO_2 nano-microsphere templates with diameters within 400 ~ 500 nm are evenly dispersed with a smooth surface (**Figure S1a**), while the smooth N—C HNMs derived from the SiO_2@PDA were shown in **Figure S1b**.

In addition, Fig. 2a and b display the TEM images of N—C HNMs and SnO_2 HNMs, where the corresponding thicknesses are ~ 17 nm and 20 nm, respectively. As observed distinctly in Fig. 2c, the TEM image proves that SnO_2 shells covered outside the N—C shell supporter construct a hollow and bilayer structure with a total thickness of ~ 30 nm. Herein, the increased thickness of the composites indicates that the interfacial interactions facilitated the adsorption of tin ions on the N—C shells. Besides, the N—C@SnO_2 HNMs consist of numerous sponge-like blocks of SnO_2 nanocrystals with permeable pores or channels, while the hollow carbon shell presents the improved conductivity for the electrochemical catalytic actions because of the nitrogen doping [35]. Furthermore, the HRTEM analysis of N—C@SnO_2 HNMs in Fig. 2d exhibits clear lattice fringes, and the lattice spacings of 0.33 nm correspond to the $(1\,1\,0)$ facets of SnO_2 [36] as observed in XRD patterns (Fig. 2e), and the corresponding elemental mapping analysis under SEM observation also clearly demonstrates the homogeneous distribution of C, N, Sn and O elements in the N—C@SnO_2 HNMs (**Figure S2**). Moreover, the Sn and C elements in the mapping image could indicate that the N—C was in inner layer while SnO_2 in the outer layer. Further, TGA analysis of the N—C@SnO_2 HNMs was performed under an air atmosphere to measure the carbon content in the composite, and the result revealed the precise content of the N—C shell as 0.8 wt% (**Figure S3**). Besides, the BET technique was used to investigate the specific surface area and porous characteristics of our product. As shown in **Figure S4**, the isotherm can be assigned to the type-IV class with hysteresis loops,

indicating the mesoporous structures. The high surface area of N—C@SnO_2 (91.01 m^2/g) provides a large number of adsorption sites for the target molecules.

Both the XRD patterns (Fig. 2e) of the N—C@SnO_2 HNMs and SnO_2 HNMs display-three peaks at $2\theta = 26.5°$, $33.8°$, and $51.8°$, matching well with the $(1\,1\,0)$, $(1\,0\,1)$, and $(2\,1\,1)$ planes, respectively of the cassiterite-tetragonal phase structure of SnO_2 (JCPDS file No. 41-1445), thus indicating the successful synthesis of the SnO_2 HNMs. However, there is no characteristic diffraction peak of graphene or graphite state carbon structures for the hybrid sample at 26°, which is due to the overlapping with the broad peak $(1\,1\,0)$ of SnO_2 [37]. Further, as shown in Fig. 2e, the broad bulge peak appearing in N—C corresponds to the amorphous hollow N—C shell obtained in Fig. 2a (inset). Finally, Fig. 2f shows the FTIR of the N—C@SnO_2 product and the appeared peaks of the carbon functional groups corresponding to the C—H (970 cm^{-1}) and C=N (1640 cm^{-1}) of the inner N—C layer [38]. Likewise, the band at 615 cm^{-1} could be assigned to the presence of the SnO_2 [39], implying the successful coating of the SnO_2 on the N—C shell, and the undried water molecules also contributed to the strong and broad peak at 3400 cm^{-1}.

The surface elemental compositions and chemical valences of N—C@SnO_2 HNMs were investigated by employing XPS characterization (Fig. 3). The survey XPS spectrum reveals the coexistence of Sn, O, C, and N elements in N—C@SnO_2 HNMs (**Figure S5**). In Fig. 3a, the XPS spectrum of Sn 3d on pure SnO_2 HNMs displays two peaks at about 495 and 486.5 eV, belonging to Sn $3d_{3/2}$ and Sn $3d_{5/2}$, respectively [36]. At the same time, similar profiles of Sn $3d_{5/2}$ and $3d_{3/2}$ were also detected on the N—C@SnO_2 HNMs with a visibly blue-shifted (~0.8 eV) compared to the pure SnO_2, indicating the electronic coupling between Sn and C elements [30]. It is noteworthy that the Sn-C bond was fitted in the Sn 3d spectrum of N—C@SnO_2 HNMs and therefore suggested a strong electron interaction between SnO_2 and N—C bilayers [28]. As a result, the electrons can flow along the N—C easily and transfer rapidly to the SnO_2 shell through the Sn-C bond.

The peak in the O1s spectrum was deconvoluted into three peaks located at 531.2, 532.7, and 533.8 eV in Fig. 3b. Herein, the prominent peak of the 531.2 eV corresponds to the lattice oxygen bound to Sn in the SnO_2 crystal, while the peak centered at 532.7 eV represents the non-stoichiometric oxygen, and the peak located at 533.8 eV can be assigned to the chemisorbed oxygen species (O_2^-) [40]. It is worth noting that the occurrence of the chemical bond might be attributed to the high energy and unsaturated state of the surface Sn atoms caused by the non-stoichiometric oxygen [28].

In addition, the XPS spectrum of C 1 s in Fig. 3c was fitted into 5 peaks at about 283.6, 284.6, 285.6, 286.8, and 289.1 eV, which could be ascribed to C-Sn, C—C/C=C, C — N, C—O, and C=O, respectively. It is worth noting here that the C – Sn bond is shown in the C 1 s spectrum by comparison with pure SnO_2, suggesting a strong electron interaction between SnO_2 and N—C in N—C@SnO_2. The existence of the C—N peak further confirms the presence of nitrogen in the composite. Moreover, as shown in Fig. 3d, three peaks in the N 1 s correspond to the pyridinic-N (398.6 eV), pyrrolic-N (400.5 eV), and oxidized-N (402.5 eV) [41]. Consequently, the pyridinic-N and pyrrolic-N can promote the electrical conductivity of the composites due to their planar structure in the carbon matrix [42].

In previous reports, the narrowing of the bandgap can increase electronic conductivity. Thus, the bandgap energy of the obtained materials was investigated through UV–vis diffuse reflectance spectroscopy (Fig. 3e, f). Obviously, the absorption edge of N—C@SnO_2 HNMs shifts to ~456 nm and ~358 nm for that of the SnO_2 HNMs. The corresponding trailing absorption of the N—C@SnO_2 HNMs runs from ~350 to 800 nm, as observed in the UV–vis spectrum (Fig. 3e). And as expected, the bandgap energy reduces from 3.68 to 3.37 eV in the SnO_2 and N—C@SnO_2 HNMs (Fig. 3f). The narrowing of the bandgap can be attributed to the combination of N—C and SnO_2, which could reduce the electron transition energy from the valence to the conduction band, thus can improve the conductivity of the materials [43].
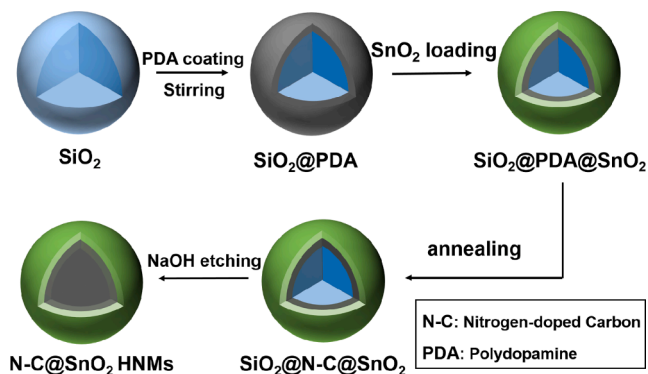
Fig. 1. (a) Schematic illustration of the preparation process of the N—C@SnO_2 HNMs catalyst.
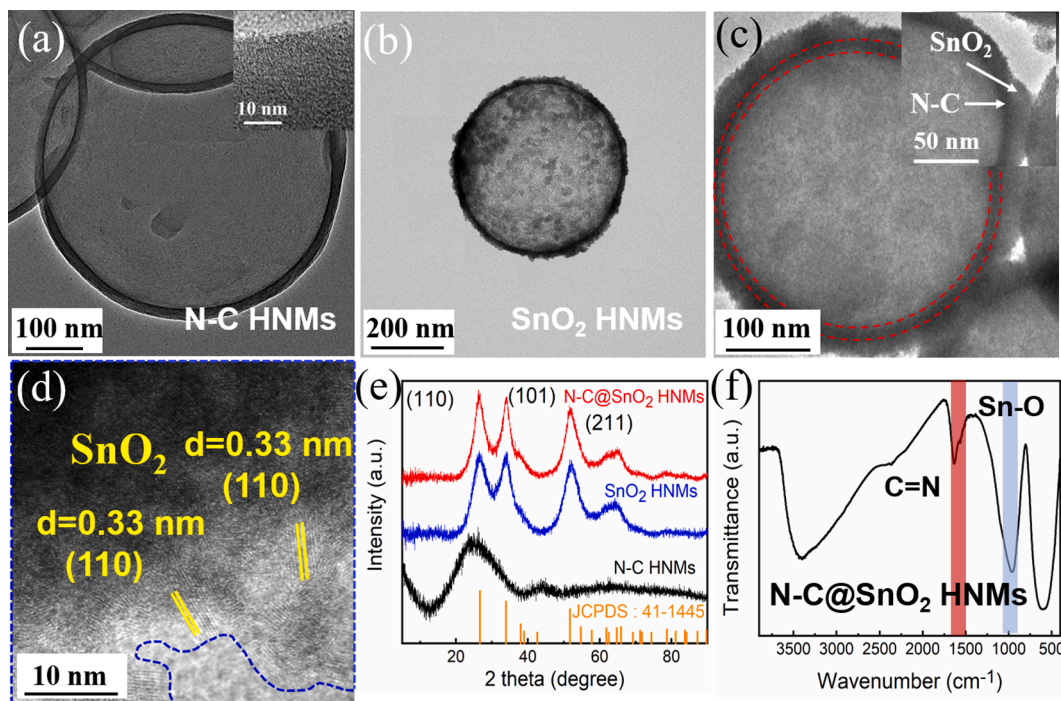
Fig. 2. (a) TEM image and HRTEM image (inset) of N—C HNMs. TEM images of (b) SnO₂ HNMs and (c) N—C@SnO₂ HNMs. (d) HRTEN image of N—C@SnO₂ HNMs; (e) XRD patterns of N—C@SnO₂ (red), SnO₂ (blue), and N—C (black) HNMs; (f) FT-IR spectrum of N—C@SnO₂ HNMs.
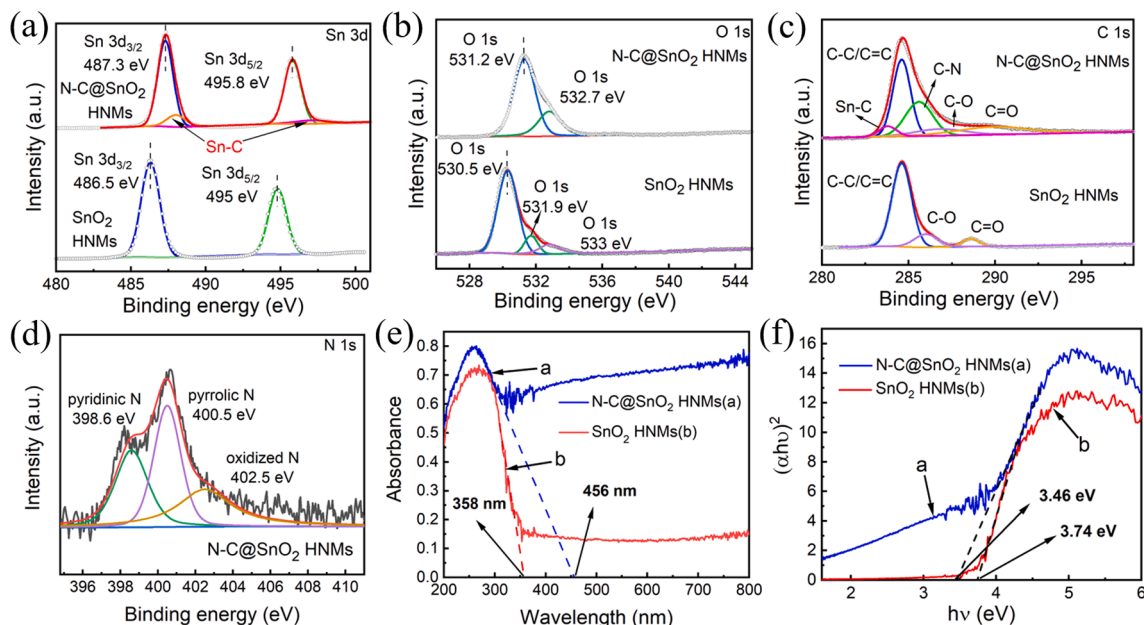
Fig. 3. XPS spectra of (a) Sn 3d, (b) O 1 s, (c) C 1 s in N—C@SnO₂ and SnO₂ HNMs. (d) N 1 s in N—C@SnO₂ HNMs; (e) UV–vis diffuse reflectance spectra of N—C@SnO₂ (blue) and SnO₂ HNMs (red); (f) Band gaps achieved from UV–vis DRS.

3.2. Electrochemical characterization of modified electrodes

To demonstrate the charge transfer kinetics properties, the EIS was carried out in the form of the Nyquist plot. Generally, the Nyquist plot comprises a semicircle in the high-frequency region and a straight line in the low-frequency region. More particularly, the semicircle diameter of the high-frequency region means the charge transfer resistance (R_{ct}) [44,45]. As shown in Fig. 4**a**, the interface R_{ct} values in the high-frequency region of the bare GCE, SnO₂, and N—C@SnO₂ electrodes are about 36.9, 826.9, and 169.2 Ω, respectively. The difference

between the bare GCE and modified GCEs indicated that the electrode materials were successfully modified on the GCE, while the drastic decrease of R_{ct} from SnO₂ to N—C@SnO₂ means that the conductivity of the material has been dramatically improved due to the high conductivity of the N—C layer, which may hold great promise to improve the electrochemical performance.

To further determine the electrocatalytic performance of the obtained electrode materials, the CV test was conducted in 250 μM DA with 0.1 M PBS at a scan rate of 50 mV s^{-1} (Fig. 4**b**), and the curves recorded from the bare GCE, SnO₂ and N—C@SnO₂ modified GCE shows that the
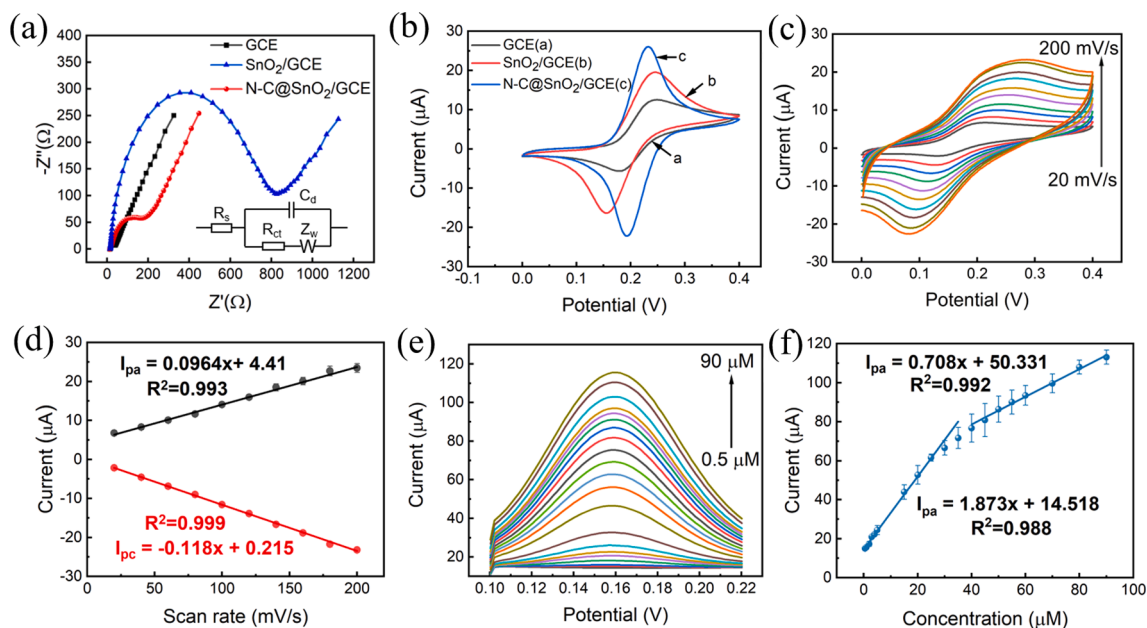
Fig. 4. (a) Nyquist plots of EIS of N—C@SnO$_2$ HNMs (red), SnO$_2$ HNMs (blue), and GCE (black) in 5 mM [Fe(CN)$_6$]$^{3-/4-}$ at 1×10^{-1} Hz to 1×10^3 kHz; (b) CV curves of N—C@SnO$_2$ HNMs (blue), SnO$_2$ HNMs (red), and GCE (black) in 0.1 M PBS (pH = 7.4) containing 250 μM DA; (c) CV response of 250 μM DA on the N—C@SnO$_2$/GCE at 0.1 M PBS (pH = 7.4) at different scan rates (20 to 200 mV s^{-1}); (d) Linear plot of peak current *vs* scan rate; (e) SWV curves of DA (0.5 to 90 μM) at N—C@SnO$_2$/GCE in 0.1 M PBS at 50 mV s^{-1}, and (f) the corresponding linear plots of cathodic peak currents *vs* DA concentration for N—C@SnO$_2$/GCE.

N—C@SnO$_2$ exhibits the highest catalytic activity compared to the GCE and the SnO$_2$, due to the highest peak current intensity for the electrochemical reactions of DA. Causes for this result might be that the heterojunction enhanced the electrocatalytic process due to the high electrical conductivity and the strong interaction of the interfacial Sn-C bond (as observed in Fig. 3a), enabling the rapid transmission of electrons of the DA electrochemical detection [46].

It is necessary to explore the optimal electrochemical test conditions, such as the volume of the electrode material and the electrolyte's acidity [47]. As is shown in **Figure S6a**, the optimization experiment of the volume of the electrode material was carried out to optimise the performance of the electrode, and the highest current peak was observed at a drop of 5 μL of the suspension. The effect of varying pH (6.8 ~ 8.0) on the electrochemical responses of the N—C@SnO$_2$/GCE towards the detection of DA has been shown in **Figure S6b**. It can be seen that the oxidation peak current of DA reaches a maximum at pH 7.4 and then decreases gradually with an increase of pH value. Thus, solution pH = 7.4 was taken for the following electrochemical test.

Different scan rate (20–200 mV·s^{-1}) performances were employed in 0.1 M PBS (pH = 7.4) containing 250 μM DA to investigate the electrocatalytic kinetic response of N—C@SnO$_2$/GCE toward DA using the CV method (Fig. 4c). The results demonstrate that the oxidation peak and reduction peak current of DA is linearly related to scanning rates (20 to 200 mV·s^{-1}). Besides, a straight-line relationship between the peak current of DA and the scan rate was observed in Fig. 4d. The linear regression equation of.

$$I_{pa} \text{ (μA)} = 0.0964x + 4.41 \text{ with } R^2 = 0.994 \quad (1)$$

and I_{pc} (μA) = -0.118x + 0.^{215} with the $R^2 = 0.999$ (2)

were obtained, which implied a surface-controlled electrochemical process of DA on N—C@SnO$_2$/GCE electrode [16]. Hence, the obtained results indicated obviously that the N—C@SnO$_2$/GCE with satisfying electrical conductivity exhibited rapid charge-transfer capability and mass transport properties.

Furthermore, SWV measurements were conducted to calculate the sensitivity and LOD of DA sensing at N—C@SnO$_2$ in the presence of 0.1 M PBS (pH = 7.4). As shown in Fig. 4e, the SWV response of N—C@SnO$_2$

to DA molecule exhibits a significant increase with the various amounts of DA solution (0.5–90 μM). It can be seen that N—C@SnO$_2$/GCE electrode displays good electrocatalytic performances toward DA. Besides, well-linear relationships were obtained between the curves of current responses and DA concentration in the detection ranges of 0.5–90 μM, as shown in the following equations.

$$I_{pa} \text{ (μA)} = 1.873x + 14.518 \text{ } (R^2 = 0.988) \text{ } (0.5 \sim 35 \text{ μM}) \quad (3)$$

$$I_{pa} \text{ (μA)} = 0.708x + 50.331 \text{ } (^{R^2} = 0.992) \text{ } (40 \sim 90 \text{ μM}) \quad (4)$$

The LOD obtained in the present study is as low as 41.5 nM, which is similar to or even lower than many other reported values shown in Table 1. The outstanding electrochemical properties of N—C@SnO$_2$ HNMs to the electrochemical oxidation of DA could be attributed to its structure in which the strong electronic coupling between SnO$_2$ and N—C leads to enhanced properties such as good conductivity and electrochemical activity during the detection of DA.

Table 1
Comparison of LOD and linear range of different modified electrodes for DA sensing.

Electrode	Linear range (μM)	LOD (μM)	References
GQDs-MWCNTs	0.005–100.0	0.87	[12]
PANI-GO	2–18	0.50	[48]
SWCNH	0.2–3.8	0.06	[49]
Nafion/MWCNT	0.1–10	0.20	[50]
MWCNT	20–50	1.07	[51]
pGr-MWCNTs-Au	1.0–100.0	0.07	[52]
Au-MWCNTs	0.48–5.7	0.071	[53]
Au@NAC-MWCNTs	0.1–250.0	0.3	[54]
ZnO/GCE	0.1–16	0.04	[55]
Au@ZIF-8	0.1–50	0.01	[56]
Cu/ZnO/GCE	0.1–20	0.055	[57]
CsZnO–PANI/GCE	20–180	0.21	[58]
GCE/CQDs/CuO	1–180	25.4	[59]
La-doped MTO/GCE	5–50	1.32	[60]
N—C@SnO$_2$ HNMs	0.5–35	0.041	This work
	40–90		

There is no doubt that the selectivity of electrochemical detection is a crucial factor in evaluating its performance. To explore the selectivity property of the N—C@SnO$_2$/GCE electrode toward DA, the electrochemical behavior of coexistence of interfering compounds in biological systems such as AA, UA, Cys, Glu, and GSH were investigated by the SWV method. As shown in **Figure S7a, b**, the current response is the highest at 250 μM DA, while there are almost no amperometric responses to other species, despite their concentrations are two times higher than that of DA. The results demonstrated an excellent selectivity ability of the N—C@SnO$_2$/GCE electrode toward the DA. Aside from the selectivity, the stability of the electrochemical sensor is another important index for evaluating the performance of electrochemical sensing [61]. As presented in **Figure S7c, d**, no apparent changes can be seen in the peak current densities after 5 consecutive cycles, which reveals the excellent cyclic stability of the N—C@SnO$_2$/GCE for detecting DA. The above results may be due to the excellent stability of the bilayered hollow hybrid and the synergistic effect between the interfaces. These results indicate that the N—C@SnO$_2$/GCE electrode holds a satisfactory application in DA detection.

3.3. Mechanism analysis of N—C@SnO$_2$ HNMs

The DFT calculations were performed to reveal the improved mechanism of electrochemical properties of the N—C@SnO$_2$-based sensor, which could be related to the interfacial Sn-C bond between the hybrid phases of the SnO$_2$ and N—C layer promote the rapid transfer of electrons through the heterointerface. The above XPS spectrum of Sn 3d and C 1s in N—C@SnO$_2$ (Fig. 3**a**) has proved the existence of Sn-C bond in the composite materials. Therefore, in this work, the models of complex structures of SnO$_2$ and N—C were taken into account, wherein the Sn-C bond was caused by the unsaturated state of the surface Sn atoms generated from the oxygen vacancies, as shown in Fig. 3**b**. It is worth pointing out that both pyrrole nitrogen and pyridine nitrogen were introduced into the N—C material, promoting the formation of the Sn-C bond [27]. As a result, the terminated Sn atom of the unsaturated state will tend to form the distorted chemical bond with the defect C atom in the carbon surface, which was caused by the N atom in the N—C shells [28].

Accordingly, the top and side views of the hybrid structure (N—C@SnO$_2$) were illustrated in Fig. 5**a** with the Sn-C bond in the interface. As shown in Fig. 5**b**, the electron transfer mechanism can be revealed by the three-dimension charge density difference. The existence of the interfacial chemical bond could act as the contributor to interfacial interaction and allow the rapid transportation of electrons between the N—C shell and SnO$_2$ shells to improve the property of electrochemical detection [29]. Thus, on the one hand, the electron transfer occurs between the N—C and SnO$_2$ shells in the interfacial layered structure; on the other hand, the generated C shells can play as a good conductor for charge transfer. It must be proposed that the prepared catalyst presents a hollow structure and porous carbon layer, thus increasing both the conductivity for electron communication and the electrochemical active surface area of the catalysts [62]. These findings can be helpful in explaining the enhanced electrochemical performances.

Based on the above experiments and theoretical calculation results, it is reasonable to imagine that the electrochemical processes were as follows. On one hand, the DA molecules were adsorbed on the electrode material due to the large surface area of the carbon and SnO$_2$ layers. The nonstoichiometric oxygen of the SnO$_2$ surface is an essential tool for the adsorption process. On the other hand, the catalytic processes occurred on the surface and heterojunction, and the sn-C bond between the hybrid phases of SnO$_2$ and N—C layers is essential for this process. The rapid electron transfer could boost the electrochemical catalytic process, thus fundamentally promote current peak and lesser potential during the detection of DA.
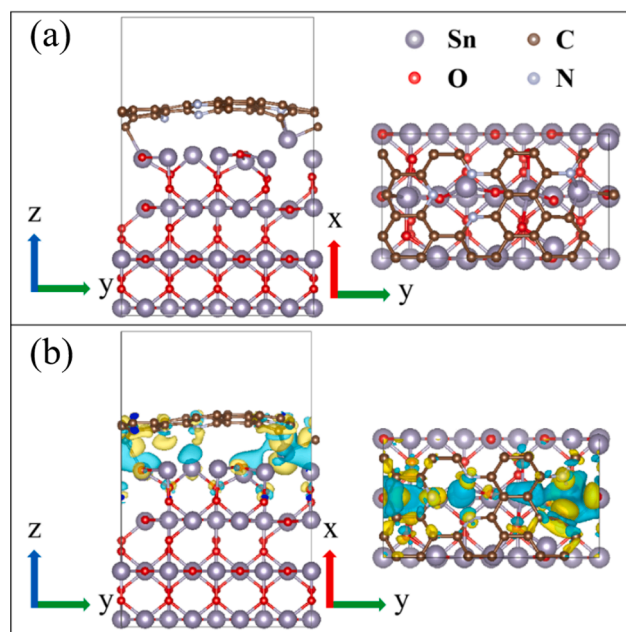
Fig. 5. (a) Geometrically optimized model of N—C@SnO$_2$ structure with strong sn-C bond. (b) Charge density difference for the N—C@SnO$_2$ model, the yellow and blue clouds represent the charge dissipation and charge accumulation, respectively.

3.4. Electrochemical detection of DA with the sensor

With improved living standards, electrochemical sensors, which could achieve in-situ detection and real-time feedback, are needed to provide more convenience for people [63]. To this end, we used the artificial sweat which contains the same amount of DA as the real sweat to simulate the portable detection of DA through assembling the N—C@SnO$_2$ electrode materials with the portable microsensor.

To prove the advantages of N—C@SnO$_2$ as a promising candidate material to realize the portable detection of DA, we coated our materials on a chip that has integrated three electrodes and is connected to an electrochemical workstation (Fig. 6**a, b**). As shown in Fig. 6**c**, the CV method was used to test sensitivity ability by dropping artificial sweat with the addition of DA on the chip. The result showed that there was a prominent oxidation peak of the N—C@SnO$_2$/gold electrode, and the well-linear relationships have been obtained between the curves of current responses and DA concentration in the detection ranges of 20 μM to 1.4 mM, as shown in Fig. 6**d**, which demonstrates a regression equation of I$_{pa}$ (μA) = 0.0611x + 1.456 with R^2 = 0.981.

In addition, the N—C@SnO$_2$ sensor was capable of detecting DA in artificial sweat with the addition of the interfering compounds in biological systems to simulate the bio-complex sample. As shown in Fig. 6**e**, there was an apparent current peak of DA while no current peak of the other compound, even with the twice concentration than that of DA. Moreover, in Fig. 6**f**, the sensor was used consecutively for 5 times without significant current change, suggesting good cycle stability. Hence, the outdoor or *in situ* detection can be realized based on such kind of electrochemical sensor [64,65].

4. Conclusions

In summary, the high-performance N—C@SnO$_2$ HNMs hybrid materials were synthesized guided by the introduction of interfacial sn-C bond with synergistic effect, and the obtained material delivered superior performances as electrode materials in the detection of DA, such as LOD of 41.5 nM, wider linear detection range from 0.5 to 90 μM and remarkable selectivity towards DA. The reason could be attributed to the
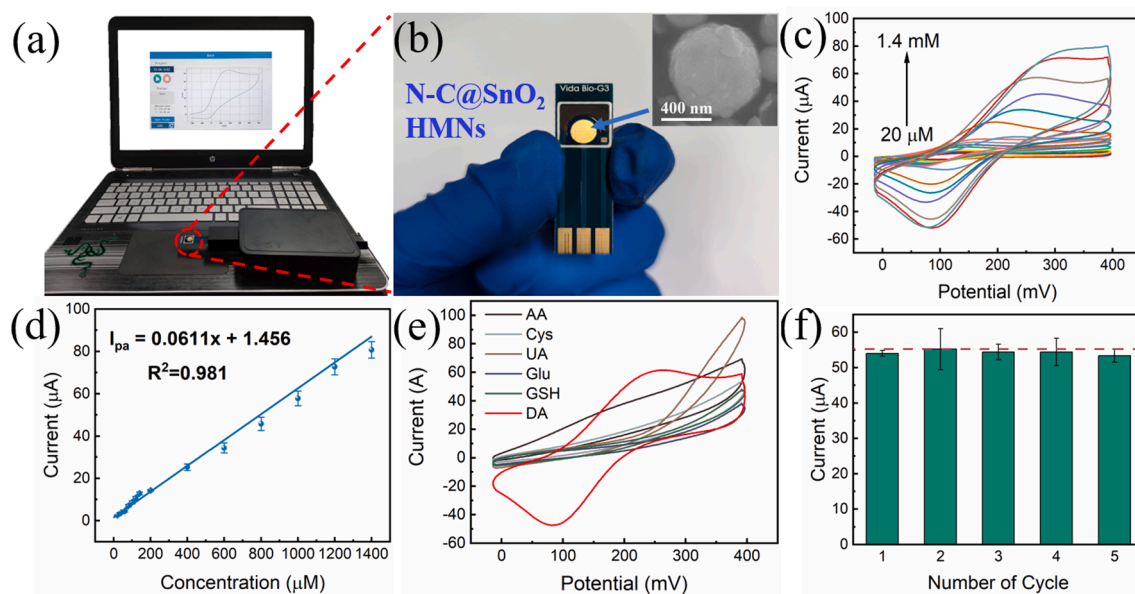
Fig. 6. (a) The MEC-VS1 Electrochemical Workstation at work; (b) The FR-4 Printed three-electrodes. (c) CV curves DA (20 μM to 1.4 mM) at N—C@SnO$_2$/gold in artificial sweat at 50 mV s^{-1}, and (d) the corresponding linear plots of oxidation current peak currents *vs* DA concentration for N—C@SnO$_2$/gold. (e) Selectivity of N—C@SnO$_2$/gold toward DA and (f) CV responses of the cyclic stability of N—C@SnO$_2$/gold in 1 mM DA at 5 cycles.

combination of the hollow SnO$_2$ and N—C components, which can improve the conductivity of the material, and the chemical bond facilitates the fast charge transfer. And then, DFT calculations demonstrated that the presence of the sn-C bond could cause charge redistribution and served as a medium for charge transfer to promote the conductivity of the N—C@SnO$_2$, leading to improved electrochemical performances than pure SnO$_2$ HNMs. Moreover, a portable microsensor based on the obtained N—C@SnO$_2$ HNMs material has been applied to the *in situ* electrochemical detection of DA in artificial sweat, and the satisfactory results such as wide detection range, favorable DA selectivity, and stable circularity illustrated it a promising candidate for the biosensor. In brief, this work not only provided a simple synthesis strategy of the hybrid structure with interfacial synergistic chemical bond but also offered insight into the design of microsensor devices.

CRediT authorship contribution statement

Kungang Chai: . **Shizhao Zhang:** Investigation, Data curation. **Hongjie Liu:** Software, Validation. **Shaopeng Wang:** Software, Validation. **Zhenghua Chen:** Software, Validation. **Kefu Yu:** Software, Validation. **Liwei Wang:** Supervision.

Declaration of Competing Interest

The authors declare that they have no known competing financial interests or personal relationships that could have appeared to influence the work reported in this paper.

Data availability

Data will be made available on request.

Acknowledgment

Appendix A. Supplementary data

Supplementary data to this article can be found online at https://doi.org/10.1016/j.apsusc.2022.154300.

References

[1] J.M. Savitt, V.L. Dawson, T.M. Dawson, Diagnosis and treatment of parkinson disease: molecules to medicine, J. Clin. Invest. 116 (2006) 1744–1754, https://doi.org/10.1172/JCI29178.
[2] J. Segura-Aguilar, I. Paris, P. Muñoz, E. Ferrari, L. Zecca, F.A. Zucca, Protective and toxic roles of dopamine in Parkinson's disease, J. Neurochem. 129 (2014) 898–915, https://doi.org/10.1111/jnc.12686.
[3] S. Latif, M. Jahangeer, D. Maknoon Razia, M. Ashiq, A. Ghaffar, M. Akram, A. El Allam, A. Bouyahya, L. Garipova, M. Ali Shariati, M. Thiruvengadam, M. Azam Ansari, Dopamine in parkinson's disease, Clin. Chim. Acta. 522 (2021) 114–126, https://doi.org/10.1016/j.cca.2021.08.009.
[4] I. Iftikhar, K.M.A. El-Nour, A. Brajter-Toth, Detection of transient dopamine antioxidant radicals using electrochemistry in electrospray ionization mass spectrometry, Electrochim. Acta. 249 (2017) 145–154, https://doi.org/10.1016/j.electacta.2017.07.087.
[5] Z. Lin, H. Wang, L. Hu, J. Li, J. Lin, B. Liu, Z. Zhao, Y. Rao, Simultaneous determination of N-ethylpentylone, dopamine, 5-hydroxytryptamine and their metabolites in rat brain microdialysis by liquid chromatography tandem mass spectrometry, Biomed. Chromatogr. 33 (2019) 1–8, https://doi.org/10.1002/bmc.4626.
[6] M. Klimuntowski, M.M. Alam, G. Singh, M.M.R. Howlader, Electrochemical sensing of cannabinoids in biofluids: a noninvasive tool for drug detection, ACS Sensors. 5 (2020) 620–636, https://doi.org/10.1021/acssensors.9b02390.
[7] T.O. Hara, B. Singh, Electrochemical biosensors for detection of pesticides and heavy metal toxicants in water: recent trends and progress, ACS ES&T Water. 1 (2021) 462–478, https://doi.org/10.1021/acsestwater.0c00125.
[8] L.M. Castle, D.A. Schuh, E.E. Reynolds, A.L. Furst, Electrochemical sensors to detect bacterial foodborne pathogens, ACS Sensors. 6 (2021) 1717–1730, https://doi.org/10.1021/acssensors.1c00481.
[9] S. Tajik, Y. Orooji, Z. Ghazanfari, F. Karimi, H. Beitollahi, R.S. Varma, H.W. Jang, M. Shokouhimehr, Nanomaterials modified electrodes for electrochemical detection of sudan I in food, J. Food Meas. Charact. 15 (2021) 3837–3852, https://doi.org/10.1007/s11694-021-00955-1.
[10] V. Vogiazi, A. De La Cruz, S. Mishra, V. Shanov, W.R. Heineman, D.D. Dionysiou, A Comprehensive Review: development of electrochemical biosensors for detection of cyanotoxins in freshwater, ACS Sensors. 4 (2019) 1151–1173, https://doi.org/10.1021/acssensors.9b00376.
[11] J.R. Sempionatto, I. Jeerapan, S. Krishnan, J. Wang, Wearable chemical sensors: emerging systems for on-body analytical chemistry, Anal. Chem. 92 (1) (2020) 378–396.

[12] Q. Huang, X. Lin, L. Tong, Q.X. Tong, Graphene quantum dots/multiwalled carbon nanotubes composite-based electrochemical sensor for detecting dopamine release from living cells, ACS Sustain. Chem. Eng. 8 (2020) 1644–1650, https://doi.org/10.1021/acssuschemeng.9b06623.

[13] H. Karimi-Maleh, H. Beitollahi, P. Senthil Kumar, S. Tajik, P. Mohammadzadeh Jahani, F. Karimi, C. Karaman, Y. Vasseghian, M. Baghayeri, J. Rouhi, P.L. Show, S. Rajendran, L.i. Fu, N. Zare, Recent advances in carbon nanomaterials-based electrochemical sensors for food azo dyes detection, Food Chem. Toxicol. 164 (2022) 112961.

[14] X. Xie, D.P. Wang, C. Guo, Y. Liu, Q. Rao, F. Lou, Q. Li, Y. Dong, Q. Li, H. Bin Yang, F.X. Hu, Single-atom ruthenium biomimetic enzyme for simultaneous electrochemical detection of dopamine and uric acid, Anal. Chem. 93 (2021) 4916–4923, https://doi.org/10.1021/acs.analchem.0c05191.

[15] Z. Zhou, S. Mukherjee, S. Hou, W. Li, M. Elsner, R.A. Fischer, Porphyrinic MOF film for multifaceted electrochemical sensing, Angew. Chemie - Int. Ed. 60 (2021) 20551–20557, https://doi.org/10.1002/anie.202107860.

[16] B. Mutharani, R. Rajakumaran, S.M. Chen, P. Ranganathan, H.C. Tsai, Hierarchical polyacrylonitrile-derived nitrogen self-doped 3D carbon superstructures enabling electrochemical detection of calcium channel blocker nimodipine in real human blood serum, ACS Sustain. Chem. Eng. 9 (2021) 6586–6598, https://doi.org/10.1021/acssuschemeng.0c09107.

[17] S. Xue, Q. Li, L. Wang, W. You, J. Zhang, R. Che, Copper- and cobalt-codoped CeO2 nanospheres with abundant oxygen vacancies as highly efficient electrocatalysts for dual-mode electrochemical sensing of microRNA, Anal. Chem. 91 (4) (2019) 2659–2666.

[18] L. Han, D.P. Yang, A. Liu, Leaf-templated synthesis of 3D hierarchical porous cobalt oxide nanostructure as direct electrochemical biosensing interface with enhanced electrocatalysis, Biosens. Bioelectron. 63 (2015) 145–152, https://doi.org/10.1016/j.bios.2014.07.031.

[19] T. Kokab, A. Shah, M.A. Khan, M. Arshad, J. Nisar, M.N. Ashiq, M.A. Zia, Simultaneous femtomolar detection of paracetamol, diclofenac, and orphenadrine using a carbon nanotube/zinc oxide nanoparticle-based electrochemical sensor, ACS Appl. Nano Mater. 4 (2021) 4699–4712, https://doi.org/10.1021/acsanm.1c00310.

[20] X. Wang, M. Zhao, H. Li, Y. Song, Y. Cheng, S. Chen, Introducing Schottky interface as a novel strategy for ultrasensitive nonenzymatic glucose detection, J. Electroanal. Chem. 801 (2017) 251–257, https://doi.org/10.1016/j.jelechem.2017.07.026.

[21] R. Nehru, C. Di Dong, C.W. Chen, Cobalt-Doped Fe3O4nanospheres Deposited on graphene oxide as electrode materials for electrochemical sensing of the antibiotic drug, ACS Appl. Nano Mater. 4 (2021) 6768–6777, https://doi.org/10.1021/acsanm.1c00826.

[22] M. Asif, A. Aziz, G. Ashraf, Z. Wang, J. Wang, M. Azeem, X. Chen, F. Xiao, H. Liu, Facet-inspired core-shell gold nanoislands on metal oxide octadecahedral heterostructures: high sensing performance toward sulfide in biotic fluids, ACS Appl. Mater. Interfaces. 10 (2018) 36675–36685, https://doi.org/10.1021/acsami.8b12186.

[23] X. Chen, H. Yu, Y. Gao, L. Wang, G.e. Wang, The marriage of two-dimensional materials and phase change materials for energy storage, conversion and applications, EnergyChem. 4 (2) (2022) 100071.

[24] L.A. Mercante, A. Pavinatto, L.E.O. Iwaki, V.P. Scagion, V. Zucolotto, O.N. Oliveira, L.H.C. Mattoso, D.S. Correa, Electrospun polyamide 6/poly(allylamine hydrochloride) nanofibers functionalized with carbon nanotubes for electrochemical detection of dopamine, ACS Appl. Mater. Interfaces. 7 (8) (2015) 4784–4790.

[25] M. Daizy, C. Tarafder, M.R. Al-Mamun, X. Liu, M. Aly Saad Aly, M.Z.H. Khan, Electrochemical detection of melamine by using reduced graphene oxide-copper nanoflowers modified glassy carbon electrode, ACS, Omega. 4 (23) (2019) 20324–20329.

[26] J. Xi, C. Xie, Y. Zhang, L. Wang, J. Xiao, X. Duan, J. Ren, F. Xiao, S. Wang, Pd Nanoparticles decorated N-doped graphene quantum Dots@N-doped carbon hollow nanospheres With high electrochemical sensing performance in cancer detection, ACS Appl. Mater. Interfaces. 8 (2016) 22563–22573, https://doi.org/10.1021/acsami.6b05561.

[27] X. Ren, J. Wang, D. Zhu, Q. Li, W. Tian, L. Wang, J. Zhang, L. Miao, P.K. Chu, K. Huo, Sn-C bonding riveted SnSe nanoplates vertically grown on nitrogen-doped carbon nanobelts for high-performance sodium-ion battery anodes, Nano Energy. 54 (2018) 322–330, https://doi.org/10.1016/j.nanoen.2018.10.019.

[28] F. Zhang, Y. Shen, M. Shao, Y. Zhang, B. Zhang, J. Wu, W. Zhang, A. Zhu, F. Huo, S. Li, SnSe2 Nanoparticles chemically embedded in a carbon shell for high-rate sodium-ion storage, ACS Appl. Mater. Interfaces. 12 (2020) 2346–2353, https://doi.org/10.1021/acsami.9b16659.

[29] X. Zhao, W. Cai, Y. Yang, X. Song, Z. Neale, H.E. Wang, J. Sui, G. Cao, MoSe2 nanosheets perpendicularly grown on graphene with Mo–C bonding for sodium-ion capacitors, Nano Energy. 47 (2018) 224–234, https://doi.org/10.1016/j.nanoen.2018.03.002.

[30] Q. Mo, N. Chen, M. Deng, L. Yang, Q. Gao, Metallic Cobalt@Nitrogen-Doped carbon nanocomposites: carbon-shell regulation toward efficient bi-functional electrocatalysis, ACS Appl. Mater. Interfaces. 9 (2017) 37721–37730, https://doi.org/10.1021/acsami.7b10853.

[31] W. Stöber, A. Fink, E. Bohn, Controlled growth of monodisperse silica spheres in the micron size range, J. Colloid Interface Sci. 26 (1968) 62–69, https://doi.org/10.1016/0021-9797(68)90272-5.

[32] V. Duraisamy, R. Krishnan, S.M. Senthil Kumar, N-Doped hollow mesoporous carbon nanospheres for oxygen reduction reaction in alkaline media, ACS appl. Nano Mater. 3 (2020) 8875–8887, https://doi.org/10.1021/acsanm.0c01639.

[33] J.P. Perdew, K. Burke, M. Ernzerhof, Generalized gradient approximation made simple, Phys. Rev. Lett. 77 (1996) 3865–3868, https://doi.org/10.1103/PhysRevLett.77.3865.

[34] R.A. Vargas-Hernández, Bayesian optimization for calibrating and selecting hybrid-density functional models, J. Phys. Chem. A. 124 (2020) 4053–4061, https://doi.org/10.1021/acs.jpca.0c01375.

[35] T. Zhao, R. Qian, Y. Tang, J. Yang, Y. Dai, W.I. Lee, J.H. Pan, Controllable synthesis and crystallization of nanoporous tio2deep-submicrospheres and nanospheres via an organic acid-mediated Sol-Gel process, Langmuir. 36 (2020) 7447–7455, https://doi.org/10.1021/acs.langmuir.0c01008.

[36] S. Singkammo, A. Wisitsoraat, C. Sriprachuabwong, A. Tuantranont, S. Phanichphant, C. Liewhiran, Electrolytically exfoliated graphene-loaded flame-made Ni-doped SnO2 composite film for acetone sensing, ACS Appl. Mater. Interfaces. 7 (2015) 3077–3092, https://doi.org/10.1021/acsami.5b00161.

[37] J. Etula, N. Wester, T. Liljeström, S. Sainio, T. Palomäki, K. Arstila, T. Sajavaara, J. Koskinen, M.A. Caro, T. Laurila, What determines the electrochemical properties of nitrogenated amorphous carbon thin films? Chem. Mater. 33 (17) (2021) 6813–6824.

[38] R.K. Selvan, I. Perelshtein, N. Perkas, A. Gedanken, Synthesis of Hexagonal-Shaped SnO 2 Nanocrystals and SnO 2 @C Nanocomposites for Electrochemical Redox Supercapacitors, J. Phys. Chem. C 112 (6) (2008) 1825–1830.

[39] M. Li, J. Xue, Integrated synthesis of nitrogen-doped mesoporous carbon from melamine resins with superior performance in supercapacitors, J. Phys. Chem. C. 118 (2014) 2507–2517, https://doi.org/10.1021/jp410198r.

[40] P.G. Choi, N. Izu, N. Shirahata, Y. Masuda, SnO2 nanosheets for selective alkene gas sensing, ACS Appl. Nano Mater. 2 (2019) 1820–1827, https://doi.org/10.1021/acsanm.8b01945.

[41] F. Qu, Y. Yuan, M. Yang, Programmed synthesis of Sn3N4 nanoparticles via a soft chemistry approach with urea: application for ethanol vapor sensing, Chem. Mater. 29 (2017) 969–974, https://doi.org/10.1021/acs.chemmater.6b03435.

[42] W. Ding, Z. Wei, S. Chen, X. Qi, T. Yang, J. Hu, D. Wang, L.J. Wan, S.F. Alvi, L. Li, Space-confinement-induced synthesis of pyridinic- and pyrrolic-nitrogen- doped graphene for the catalysis of oxygen reduction, Angew. Chemie - Int. Ed. 52 (2013) 11755–11759, https://doi.org/10.1002/anie.201303924.

[43] N. Wang, X. Xu, T. Liao, Y. Du, Z. Bai, S. Dou, Boosting sodium storage of double-shell sodium titanate microspheres constructed from 2D ultrathin nanosheets via sulfur doping, Adv. Mater. 30 (2018) 1–9, https://doi.org/10.1002/adma.201804157.

[44] Y. Orooji, P.N. Asrami, H. Beitollahi, S. Tajik, M. Alizadeh, S. Salmanpour, M. Baghayeri, J. Rouhi, A.L. Sanati, F. Karimi, An electrochemical strategy for toxic ractopamine sensing in pork samples; twofold amplified nano-based structure analytical tool, J. Food Meas. Charact. 15 (2021) 4098–4104, https://doi.org/10.1007/s11694-021-00982-y.

[45] B. Li, P. Gu, Y. Feng, G. Zhang, K. Huang, H. Xue, H. Pang, Ultrathin nickel-cobalt phosphate 2D nanosheets for electrochemical energy storage under aqueous/solid-state electrolyte, Adv. Funct. Mater. 27 (12) (2017) 1605784.

[46] S. Tajik, A. Lohrasbi-Nejad, P. Mohammadzadeh Jahani, M.B. Askari, P. Salarizadeh, H. Beitollahi, Co-detection of carmoisine and tartrazine by carbon paste electrode modified with ionic liquid and MoO3/WO3 nanocomposite, J. Food Meas. Charact. 16 (2022) 722–730, https://doi.org/10.1007/s11694-021-01201-4.

[47] D.S. Rajawat, N. Kumar, S.P. Satsangee, Trace determination of cadmium in water using anodic stripping voltammetry at a carbon paste electrode modified with coconut shell powder, J. Anal. Sci. Technol. 5 (2014) 1–8, https://doi.org/10.1186/s40543-014-0019-0.

[48] P. Manivel, M. Dhakshnamoorthy, A. Balamurugan, N. Ponpandian, D. Mangalaraj, C. Viswanathan, Conducting polyaniline-graphene oxide fibrous nanocomposites: Preparation, characterization and simultaneous electrochemical detection of ascorbic acid, dopamine and uric acid, RSC Adv. 3 (2013) 14428–14437, https://doi.org/10.1039/c3ra42322k.

[49] S. Zhu, H. Li, W. Niu, G. Xu, Simultaneous electrochemical determination of uric acid, dopamine, and ascorbic acid at single-walled carbon nanohorn modified glassy carbon electrode, Biosens. Bioelectron. 25 (2009) 940–943, https://doi.org/10.1016/j.bios.2009.08.022.

[50] J. Zhao, Y. Yu, B. Weng, W. Zhang, A.T. Harris, A.I. Minett, Z. Yue, X.F. Huang, J. Chen, Sensitive and selective dopamine determination in human serum with inkjet printed Nafion/MWCNT chips, Electrochem. Commun. 37 (2013) 32–35, https://doi.org/10.1016/j.elecom.2013.10.007.

[51] S.M. Ghoreishi, M. Behpour, S. Mousavi, A. Khoobi, F.S. Ghoreishi, Simultaneous electrochemical determination of dopamine, ascorbic acid and uric acid in the presence of sodium dodecyl sulphate using a multi-walled carbon nanotube modified carbon paste electrode, RSC Adv. 4 (2014) 37979–37984, https://doi.org/10.1039/c4ra04919e.

[52] C. Zhang, J. Ren, J. Zhou, M. Cui, N. Li, B. Han, Q. Chen, Facile fabrication of a 3,4,9,10-perylene tetracarboxylic acid functionalized graphene-multiwalled carbon nanotube-gold nanoparticle nanocomposite for highly sensitive and selective electrochemical detection of dopamine, Analyst. 143 (2018) 3075–3084, https://doi.org/10.1039/c8an00559a.

[53] F.R. Caetano, L.B. Felippe, A.J.G. Zarbin, M.F. Bergamini, L.H. Marcolino-Junior, Gold nanoparticles supported on multi-walled carbon nanotubes produced by biphasic modified method and dopamine sensing application, Sensors Actuators, B Chem. 243 (2017) 43–50, https://doi.org/10.1016/j.snb.2016.11.096.

[54] Z. Wang, H. Guo, R. Gui, H. Jin, J. Xia, F. Zhang, Simultaneous and selective measurement of dopamine and uric acid using glassy carbon electrodes modified with a complex of gold nanoparticles and multiwall carbon nanotubes, Sensors

Actuators, B Chem. 255 (2018) 2069–2077, https://doi.org/10.1016/j.snb.2017.09.010.

[55] D. Balram, K.Y. Lian, N. Sebastian, A novel electrochemical sensor based on flower shaped Zinc Oxide nanoparticles for the efficient detection of dopamine, Int. J. Electrochem. Sci. 13 (2018) 1542–1555, https://doi.org/10.20964/2018.02.06.

[56] S. Lu, M. Hummel, K. Chen, Y. Zhou, S. Kang, Z. Gu, Synthesis of Au@ZIF-8 nanocomposites for enhanced electrochemical detection of dopamine, Electrochem. Commun. 114 (2020), 106715, https://doi.org/10.1016/j.elecom.2020.106715.

[57] A. Anaraki Firooz, M. Ghalkhani, J.A. Faria Albanese, M. Ghanbari, High electrochemical detection of dopamine based on Cu doped single phase hexagonally ZnO plates, Mater. Today Commun. 26 (2021), 101716, https://doi.org/10.1016/j.mtcomm.2020.101716.

[58] K. Pandiselvi, S. Thambidurai, Chitosan-ZnO/polyanilne nanocomposite modified glassy carbon electrode for selective detection of dopamine, Int. J. Biol. Macromol. 67 (2014) 270–278, https://doi.org/10.1016/j.ijbiomac.2014.03.028.

[59] S.E. Elugoke, O.E. Fayemi, A.S. Adekunle, B.B. Mamba, T.T.I. Nkambule, E. E. Ebenso, Electrochemical sensor for the detection of dopamine using carbon quantum dots/copper oxide nanocomposite modified electrode, FlatChem. 33 (2022), 100372, https://doi.org/10.1016/j.flatc.2022.100372.

[60] R.R. Mathiarasu, A. Manikandan, J.N. Baby, K. Panneerselvam, R. Subashchandrabose, M. George, Y. Slimani, M.A. Almessiere, A. Baykal, Hexagonal basalt-like ceramics LaxMg1-xTiO3 (x = 0 and 0.5) contrived via deep eutectic solvent for selective electrochemical detection of dopamine, Phys. B

Condens. Matter. 615 (2021), 413068, https://doi.org/10.1016/j.physb.2021.413068.

[61] W. Li, X. Guo, P. Geng, M. Du, Q. Jing, X. Chen, G. Zhang, H. Li, Q. Xu, P. Braunstein, H. Pang, Rational design and general synthesis of multimetallic metal-organic framework nano-octahedra for enhanced Li–S battery, Adv. Mater. 33 (2021) 1–9, https://doi.org/10.1002/adma.202105163.

[62] L. Lang, Y. Shi, J. Wang, F. Bin Wang, X.H. Xia, Hollow core-shell structured Ni-Sn@C nanoparticles: A novel electrocatalyst for the hydrogen evolution reaction, ACS Appl. Mater. Interfaces. 7 (2015) 9098–9102, https://doi.org/10.1021/acsami.5b00873.

[63] S. Zheng, Q. Li, H. Xue, H. Pang, Q. Xu, A highly alkaline-stable metal oxide@metal-organic framework composite for high-performance electrochemical energy storage, Natl. Sci. Rev. 7 (2020) 305–314, https://doi.org/10.1093/nsr/nwz137.

[64] S. Tajik, Y. Orooji, F. Karimi, Z. Ghazanfari, H. Beitollahi, M. Shokouhimehr, R. S. Varma, H.W. Jang, High performance of screen-printed graphite electrode modified with Ni–Mo-MOF for voltammetric determination of amaranth, J. Food Meas. Charact. 15 (2021) 4617–4622, https://doi.org/10.1007/s11694-021-01027-0.

[65] H. Beitollahi, M. Shahsavari, I. Sheikhshoaie, S. Tajik, P.M. Jahani, S. Z. Mohammadi, A.A. Afshar, Amplified electrochemical sensor employing screen-printed electrode modified with Ni-ZIF-67 nanocomposite for high sensitive analysis of Sudan I in present bisphenol A, Food Chem. Toxicol. 161 (2022), 112824, https://doi.org/10.1016/j.fct.2022.112824.